applied sciences

MDPI

Article

Study on Shear Performance of Web-Embedded Composite Shear Connector

Xiaoqing Xu [1,2,†], Tuoying Sun [1,3,*,†], Shiao Hu [1,3], Hongmei Tan [1,3,*], Yuxiao Wang [3,4] and Yong Zeng [1,3]

[1] State Key Laboratory of Mountain Bridge and Tunnel Engineering, Chongqing Jiaotong University, Chongqing 400074, China; 21030@tongji.edu.cn (X.X.); hushiao@mails.cqjtu.edu.cn (S.H.); yongzeng@cqjtu.edu.cn (Y.Z.)
[2] School of Civil Engineering, Tongji University, Shanghai 200092, China
[3] School of Civil Engineering, Chongqing Jiaotong University, Chongqing 400074, China; wyx29531@126.com
[4] Construction Branch of State Grid Sichuan Electric Power Company, Chengdu 610056, China
* Correspondence: sunty@mails.cqjtu.edu.cn (T.S.); hmtan@cqjtu.edu.cn (H.T.); Tel.: +86-189-9694-8283 (T.S.); +86-136-3790-1868 (H.T.)
† These authors contributed equally to this work.

Abstract: Based on the existing research on connectors, a web-embedded composite shear connector was proposed in this paper. Further, six types of push-out specimens were carried out on static push-out and low-cycle repeated load tests. The failure forms, load–slip curves, and load–strain curves of the tests are analysed. On the basis of the experiment, the finite element analysis is also carried out to enlarge the parameters of the specimens. The results showed that the shear stiffness of the web-embedded composite shear connector was larger than that of pure stud shear connector or perfobond rib shear connector, the slip limit was smaller, and ductility was good. A parameter analysis showed that penetrating steel rebars have the greatest impact on ultimate shear bearing capacity, reaching 43.82% of ultimate shear bearing capacity. Following repeated loading, the ultimate shear bearing capacity of the specimen decreased, the ultimate slip increased, and the ductility decreased. Based on the experimental results of this study, a new calculation equation for the ultimate shear bearing capacity of a web-embedded composite shear connector was proposed with a finite element model for verification.

Keywords: steel–concrete composite structure; web-embedded connector; push-out test; finite element analysis; shear performance

Citation: Xu, X.; Sun, T.; Hu, S.; Tan, H.; Wang, Y.; Zeng, Y. Study on Shear Performance of Web-Embedded Composite Shear Connector. *Appl. Sci.* **2024**, *14*, 5143. https://doi.org/10.3390/app14125143

Academic Editor: Dario De Domenico

Received: 15 April 2024
Revised: 21 May 2024
Accepted: 25 May 2024
Published: 13 June 2024

1. Introduction

The stud [1–4] and perfobond rib shear connector (PBL) [5] are two types of traditional shear connectors. The PBL shear connector is rigid, whereas the stud shear connector is flexible [6]. The stud shear connector has the characteristics of convenient construction, low cost, and consistent shear resistance in all directions [7–10]. The PBL shear connector has higher shear resistance and shear stiffness, as well as having the advantages of excellent fatigue resistance and simple construction [11–16]. The web-embedded connector is a type of shear connector that effectively combines the stud shear connector and the PBL shear connector.

Web-embedded connectors originate from puzzle (PZ)-shaped composite dowel shear connectors, the removal of traditional shear connectors in case of the low utilisation of the upper flange, and the cutting of steel plates into various shapes to connect with concrete. Germany first used PZ shear connectors without a flange plate to build the Perkinger Viaduct [17], following which different types of web-embedded connectors began to appear. The yield strength of the steel rebar also changes when the fabrication process changes, which also affects the shear properties of the shear connector. When the Tempcore process is used, the yield and ultimate tensile strengths of the rebar increase [18,19].

Guoqiang [20,21] proposed a new composite beam with an embedded web, wherein the upper flange plate was removed from the structure to form a steel plate shear connector with a slot at the upper end of the web plate. The Pennsylvania Department of Transportation developed a highway bridge comprising T-shaped steel beams and penetrating rebars embedded in concrete slabs. Naito CJ [22] developed a full-scale bridge model and studied its flexural performance; the results showed that the design and manufacturing method satisfied the AASHTO limit state standard [23]. Yuanlong [24] constructed nine external U-shaped steel–concrete composite beams with an embedded web (WUSCB) and investigated the effects of the shear span ratio, concrete wing width, joint spacing and inclination angle, bottom longitudinal bar diameter, stud and stirrup setting, and U-shaped steel web height-to-thickness ratio on its shear performance.

However, the research on web-embedded connectors is insufficient, and there is no universal consensus. When considering different internal geometries, there remains considerable research space for web-embedded connectors.

Therefore, this study proposed an economical and reasonable connection web-embedded composite shear connector (WECSC) that saves construction time and improves the efficiency of WECSCs, which are directly used in web hole T-shaped steel (Figure 1). The WECSC comprises four parts: concrete, embedded steel web, penetrating rebar, and studs. In order to study the shear properties of the WECSSC, seven push-out specimens of six types with different internal structures were designed and made in this paper, and push-out tests were carried out on them, focusing on the analysis of the failure forms, load–slip curves, and load–strain curves of the tests. The specimen was simulated by ABAQUS (2022) finite element software, and an expanded parameter analysis was carried out on the basis of the test. Through experiments and finite element analysis, the failure form and force transfer mechanism of the composite shear key with embedded web are discussed, and the proportion of different shear members in the ultimate bearing capacity of the composite shear key with embedded web is expected to be obtained. In addition, considering the existing calculation equation and combining it with the test data of this study, an equation for calculating the ultimate shear bearing capacity (USBC) was proposed and verified through tests and finite element simulations. The flowchart of this paper is shown in Figure 2.

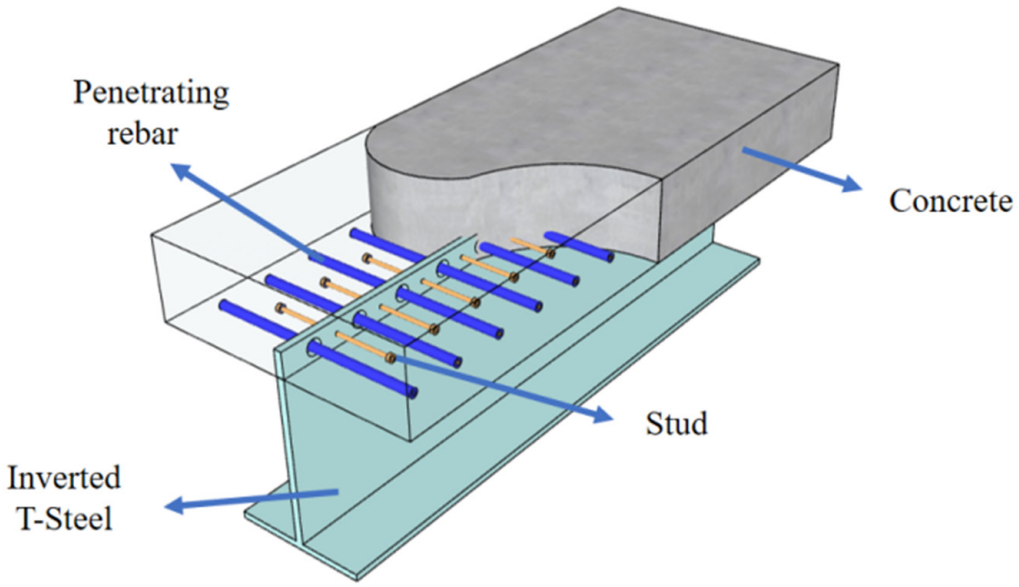

Figure 1. Structural map of WECSC.

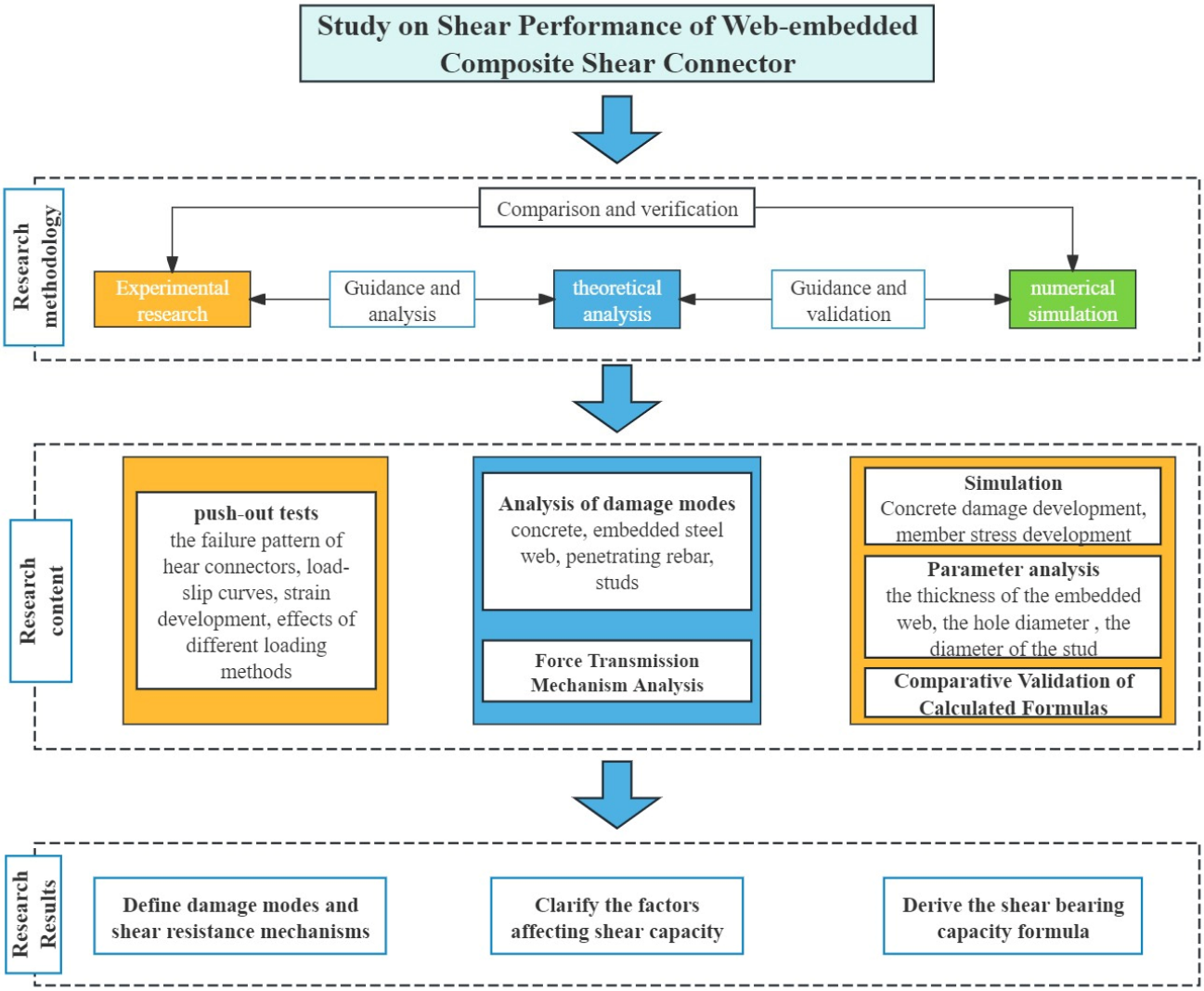

Figure 2. The flowchart.

2. Push-Out Test

2.1. Specimen Design and Manufacture

In this study, the shear properties of WECSC were analysed via a push-out test [25,26]. The concrete grade was C50, and the unilateral volume was 180 mm × 430 mm × 500 mm. To eliminate the end-bearing effect, a gap of 100 mm × 70 mm × 50 mm was set in the inner–middle part of the outsourced concrete. The hole steel web was 16 mm thick using a Q345 steel plate with dimensions of 480 mm × 320 mm and a hole diameter of 44 mm. The steel bar model was HRB400, with a length of 400 mm and diameters of 14, 18, and 22 mm, respectively. The stud was used in accordance with the literature [27], with the selected model being Ø13, composed of ML-15. Further, HRB400 steel bars with a diameter of 10 mm were selected for the stirrup. The specific structure and size of the specimen P-18-S are shown in Figure 3.

In this experiment, the sizes of the perforating steel bar, stud, and end bearing action of the WECSC were selected as the test analysis parameters (Table 1). There were seven specimens in this test, which were divided into six types. The P-0 specimens were connected to only a perforated steel plate. The P-18 specimens were connected to the steel bars. P-n-S (n = 14, 18, and 22) specimens were set to penetrate the rebar bars and stud connections. Based on the P-18-S specimens, in P-18-S# specimen, the voids in the inner middle and lower parts of the enclosed concrete were eliminated, and an end-bearing area was added.

Among them, two specimens of P-18-S were used for push-out test and low-cycle repeated load test, while the other specimens were only used for push-out test. The connection details are shown in Figure 4.

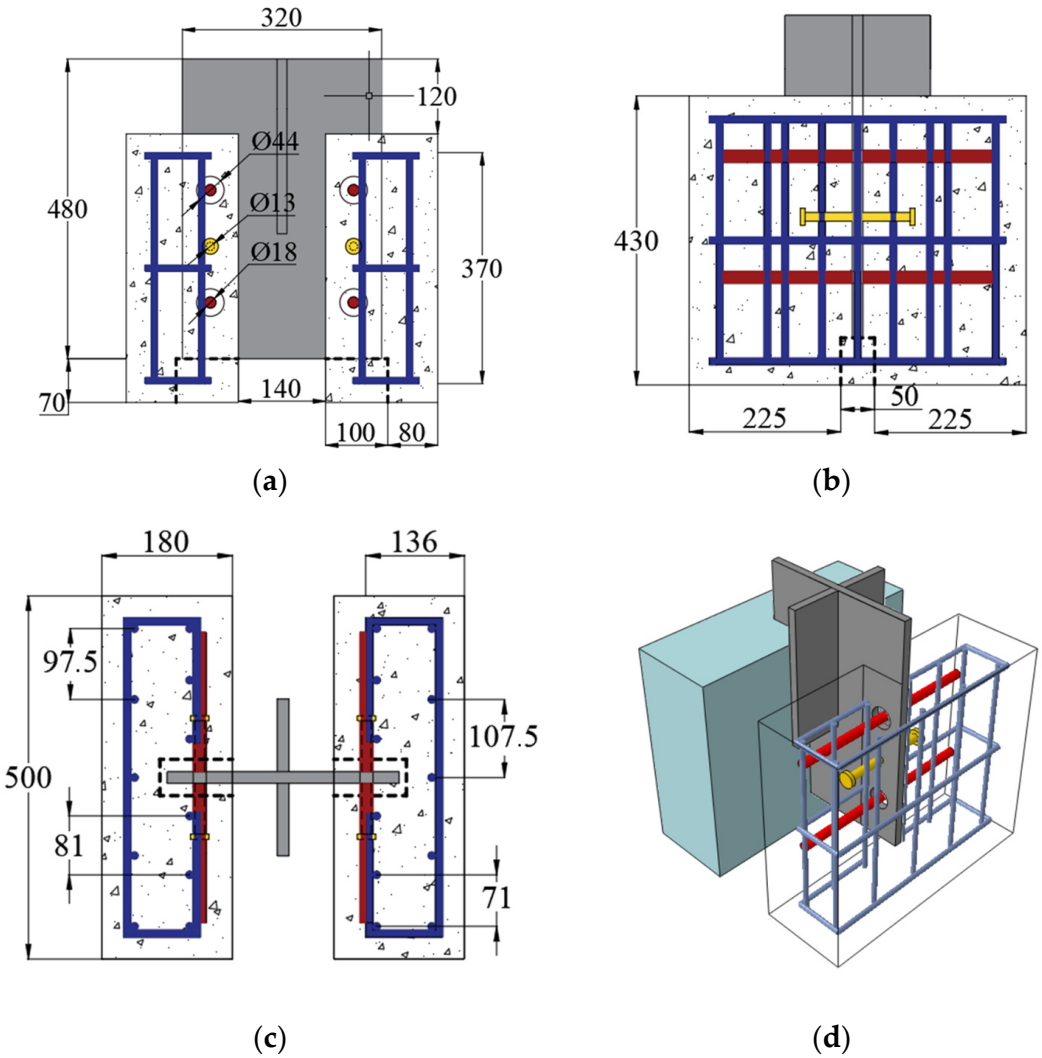

Figure 3. P-18-S specimen structure size diagram (mm). (**a**) Front view; (**b**) side view; (**c**) top view; (**d**) 3D view.

Table 1. Internal component parameters of test specimens.

Specimen Number	Concrete Label	Diameter of Penetrating Rebar/mm	Stud Type	End Pressure
P-0	C50	/	/	none
P-18	C50	18	/	none
P-18-S	C50	18	Ø13	none
P-18-S#	C50	18	Ø13	yes
P-14-S	C50	14	Ø13	none
P-22-S	C50	22	Ø13	none

The actual compressive strength of concrete was f_{cu} = 56.9 MPa, measured through the standard cube test. Parameters of steel components are presented in Table 2.

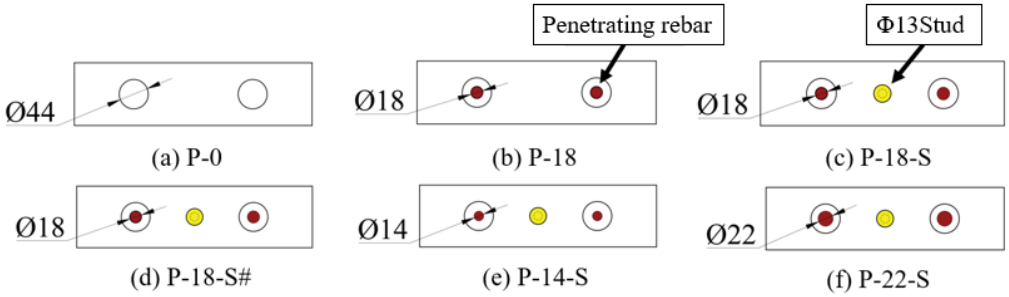

Figure 4. Six types of specimen connection details (mm).

Table 2. Steel component properties.

Material Type	Thickness/Diameter (mm)	Elastic Modulus E_s (GPa)	Yield Strength f_y (MPa)	Ultimate Strength f_u (MPa)
Q345 Steel plate	16	210	340	475
ML-15 Stud	13	206	442	525
HRB400 Steel	14	200	450	540
	18	200	450	570
	22	200	450	580

2.2. Test Device and Measurement Scheme

The device used for the push-out test is shown in Figure 5.

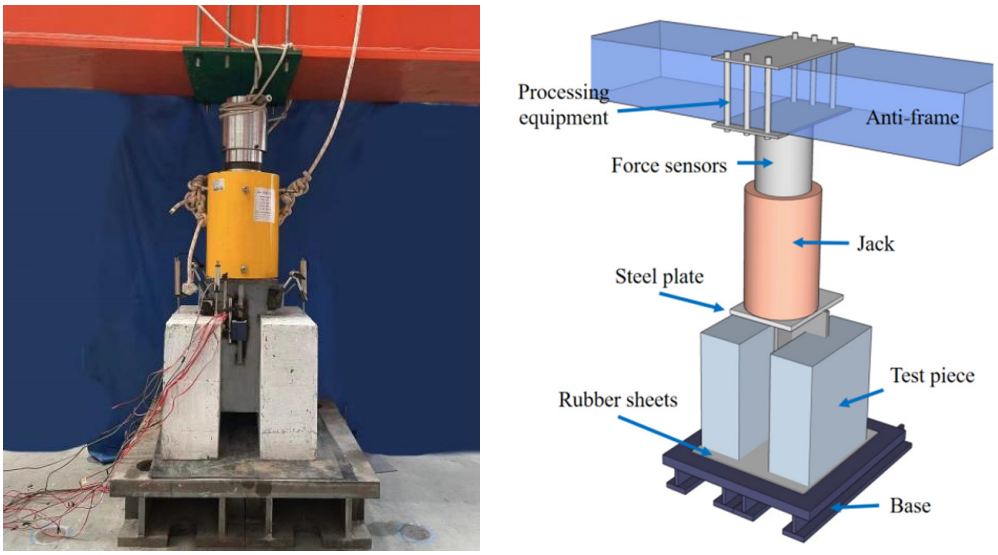

Figure 5. Specimen loading. (**a**) Specimen loading photograph; (**b**) specimen loading diagram.

(1) Push-out test

The value of the preloading was set about 0.3 times the calculated USBC, about 15 min. A combination of load and displacement control was adopted for formal loading. First, load control was used to perform graded loading: 10–20 kN at each stage in the elastic stage and 5–10 kN in the elastoplastic stage. Furthermore, the load was held for 5 min after each stage was loaded to ensure that the internal components of the specimen were fully deformed, and the outer concrete was observed for cracks. After the specimen entered the plastic stage, displacement control was chosen instead of the loading mode,

with a displacement of 0.1 mm at each stage. When the specimen reached the peak load, it continued to be loaded up to 50% of the peak load or stopped loading when the penetrating rebar broke. In this test, the loading rate was 1 kN/s and the displacement loading rate was 0.02 mm/s.

(2) Low-cycle repeated load test

Preloading was also performed before the repeated low-cycle load tests. The test adopted an increased one-way repeated load. The static push-out test showed that the slip limit of the specimen was not large. Therefore, the increment in the repeated load at each stage was controlled by the load shown in Figure 6. After the repeated loading, unidirectional loading was applied until the specimens were damaged.

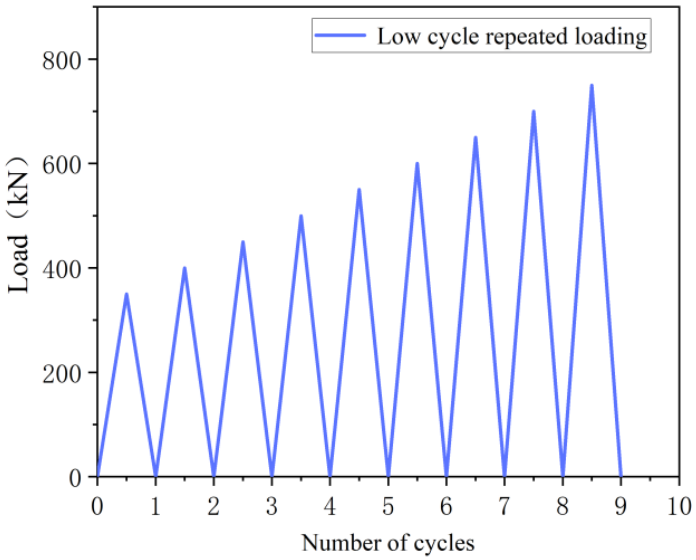

Figure 6. Specimen loading scheme.

2.3. Test Process and Failure Pattern

(1) External failure pattern

According to the failure mode of each specimen (as shown in Figure 7), the crack failure mechanism of the WECSC is as follows: (1) Vertical cracks appeared on the outer side of the concrete, extending from the bottom to the upper side. Subsequently, the cracks expanded in all directions and continued to expand vertically with a high probability, which was caused by the dilatancy effect of the compressive concrete of the specimen. (2) The cracks in the upper part of the concrete originated at the hole in the steel web and extended along the steel bar axis. (3) Oblique shear cracks appeared inside the concrete slab, generally starting at the position from where the upper row of steel bars ran through and extending diagonally downward from the steel–concrete junction. (4) The front concrete was pulled apart in the vertical direction, and the crack extended upward from the bottom, corresponding to the hole position. (5) With the development of cracks, the concrete front cracks connected with the top cracks or with the inner cracks such that the inner wall of the concrete was split off entirely. When the cracks were on the front, the inside and top three sides of the concrete were connected, network cracks formed, and the inner wall concrete fell off as a sheet piece. The development of major cracks was accompanied by the crushing of the concrete in the cracks, as well as the concrete at the bottom.

In addition, concrete cracking and spalling became increasingly evident with an increase in the internal components of the specimens. The change in the diameter of the penetrating rebar mainly affected the crack development in the top concrete. The larger the diameter, the more obvious the crack development along the penetrating rebar and the more obvious the steel–concrete separation phenomenon. Increasing the end bearing

area resulted in an increase in small cracks outside the concrete; however, it weakened the tendency of crack widening.

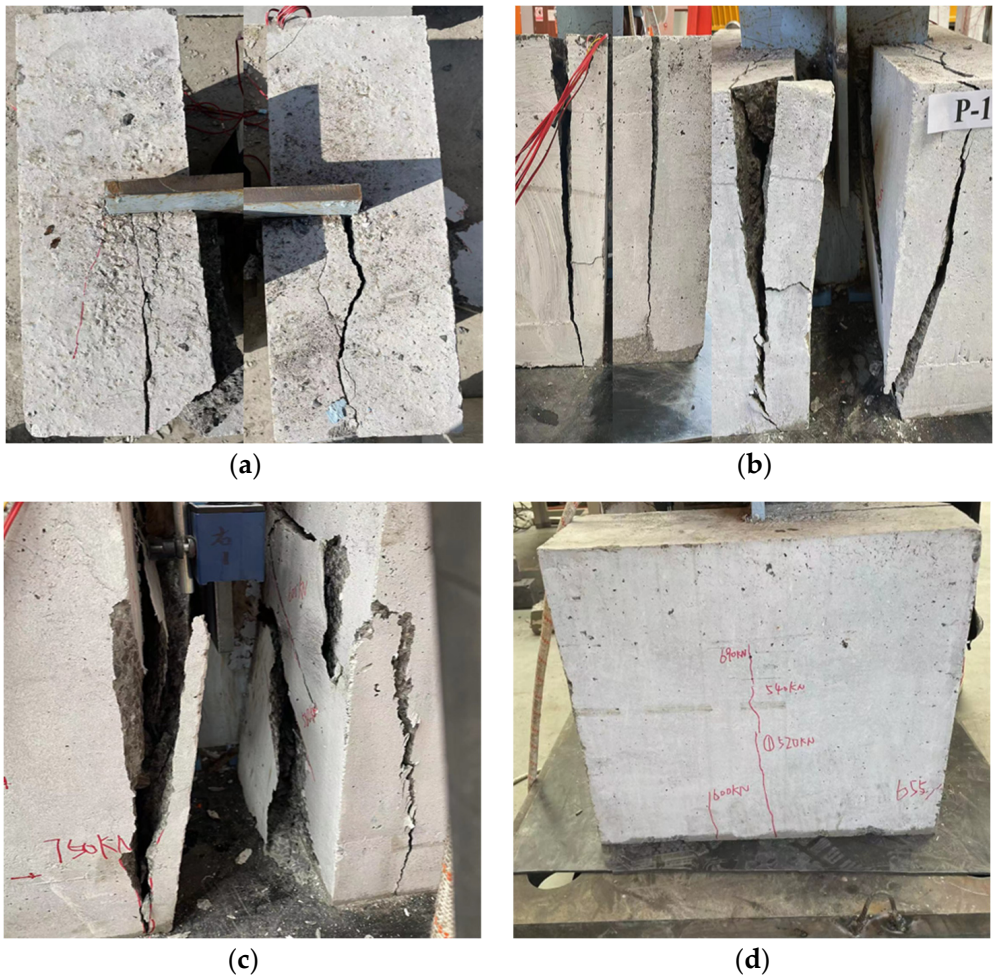

(**a**) (**b**) (**c**) (**d**)

Figure 7. Overall failure mode of P-18-S specimen in static push out test. (**a**) Specimen top; (**b**) specimen face; (**c**) inner side of specimen; (**d**) specimen outer side.

(2) Internal failure pattern

(1) Embedded steel web

As shown in Figure 8, no visible buckling deformation or plastic deformation was observed. The concrete dowel in the P-0 specimen was cut, and a certain amount of concrete broke owing to the absence of a reinforcing bar in the opening hole. The remaining steel plate holes were arranged with penetrating rebars; thus, the concrete in the holes was subjected to the joint action of embedded steel web and penetrating rebars, accompanied by shear damage.

(2) Stud

Shear failure did not occur in any of the studs because the arrangement of the stirrup resulted in the concrete restraining the studs and the reinforcement bore a part of the shear force. Consequently, all studs in the test pieces were bent and deformed at the root. The degree of stud bending in the P-14-S specimen was significantly higher than that in the P-22-S specimen because the penetrating rebar in the P-22-S specimen bore greater shear. The damage patterns of the studs are shown in Figure 9.

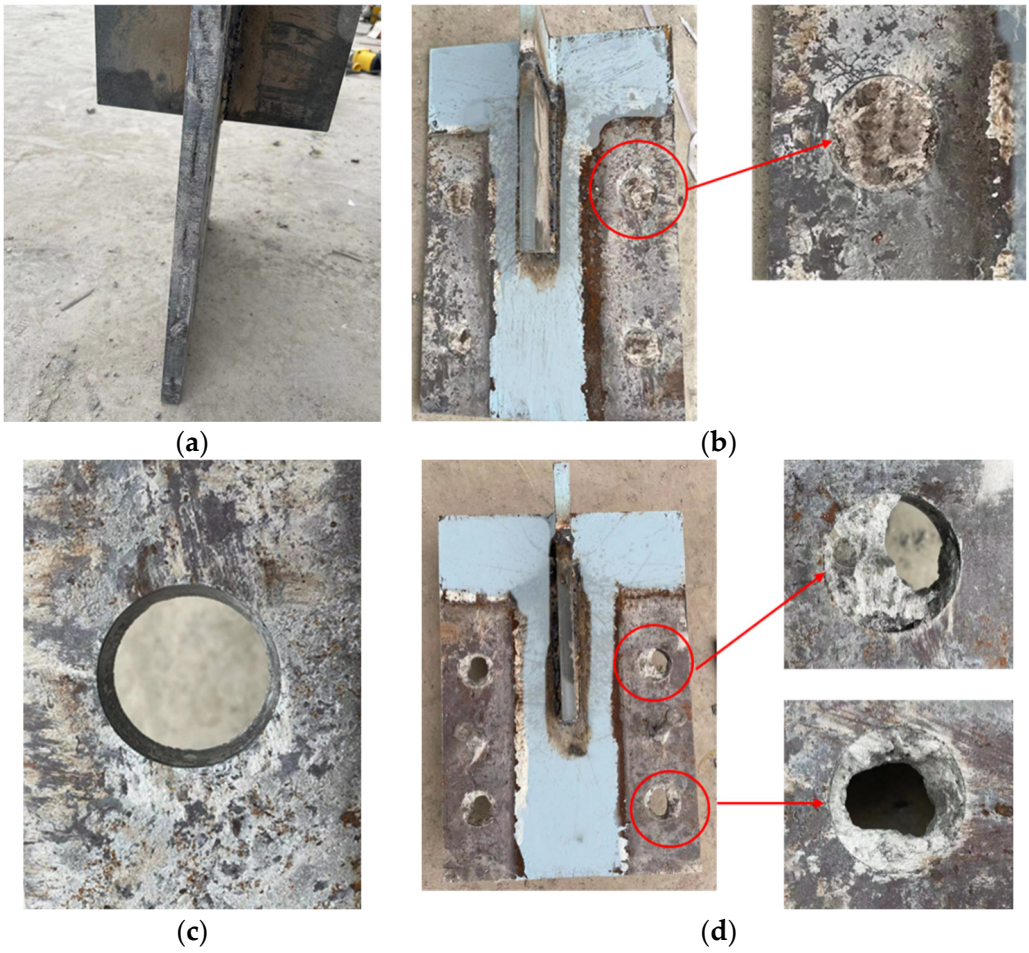

Figure 8. Damage pattern of perforated steel plate. (**a**) Steel plate is not buckling; (**b**) concrete dowel cut in the hole; (**c**) no plastic deformation; (**d**) shear failure.

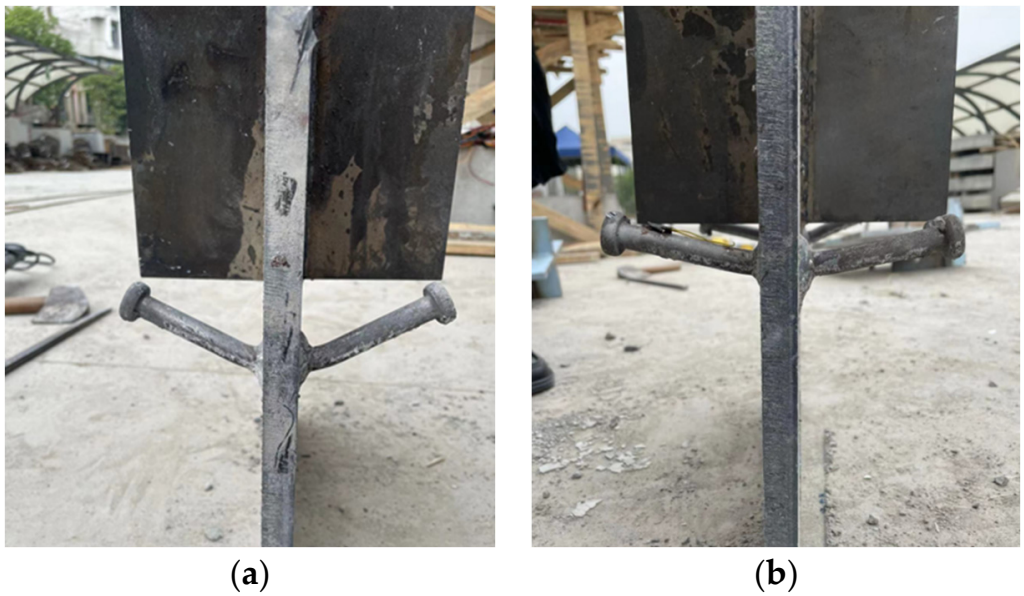

Figure 9. Stud failure pattern. (**a**) P-14-S specimen; (**b**) P-22-S specimen.

(3) Penetrating rebar

The failure mode of the penetrating rebars was flexural shear failure along the loading direction instead of shear failure. Furthermore, the degree of bending of the upper bars was higher than that of the lower bars, indicating that the upper bars exhibited higher shear degrees. Because the end-bearing area shared a portion of the shear force, the bending degree of the penetrating rebar in P-18-S# specimen was smaller than that in P-18-S, and the same was true for the other specimens. After the P-18-S specimen was subjected to a low-cycle repeated load, the curvature of the penetrating rebar decreased. The damage patterns of the penetrating rebar are shown in Figure 10.

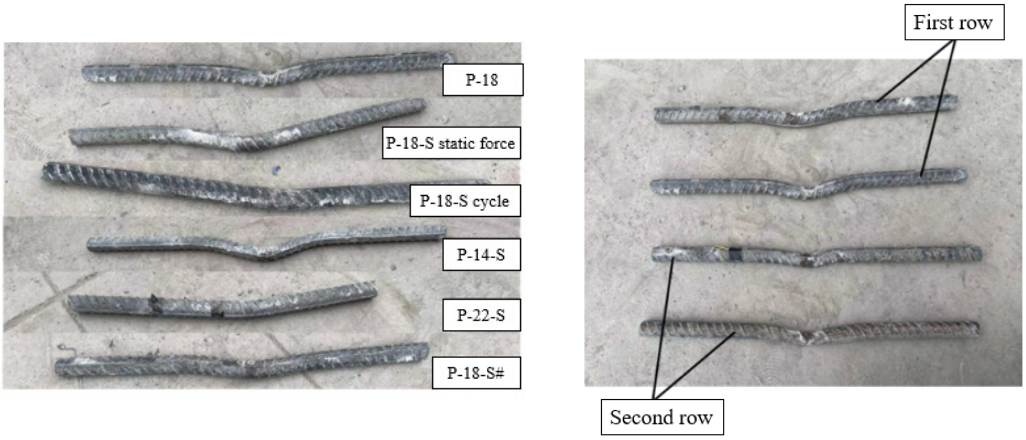

Figure 10. Damage pattern through steel bars.

2.4. Load–Slip Curve

To study the USBC of each part in the WECSC, the load–slip curves of four specimens were obtained (Figure 11). Additionally, the USBCs and corresponding displacements are listed in Table 3.

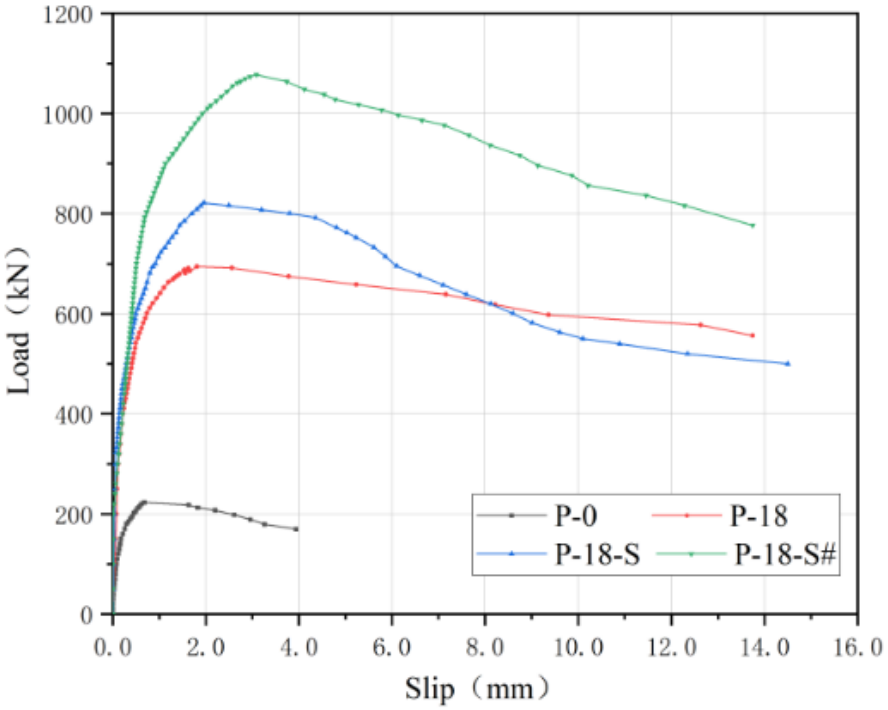

Figure 11. Load–slip curves of four different specimens.

Table 3. USBC and slippage from test result.

Specimen Number	USBC/kN	Slippage Corresponding to Peak Load/mm
P-0	223.05	0.68
P-18	694.26	1.81
P-18-S	821.43	1.96
P-18-S#	1077.5	3.09

In Figure 11, three stages were observed in the load–slip curve: elastic, nonlinear, and descending. In the elastic stage, the load changes significantly albeit with less slip, meaning that the WECSC was a rigid shear connector, and most of the load was borne by the shear capacity of the concrete dowel.

Before entering the nonlinear stage, the maximum load values of P-0, P-18, P-18-S, and P-18-S# were 150.36, 531.44, 590.16, and 700.65 kN, respectively, accounting for 67.41, 76.54, 71.84, and 65.02% of USBC, respectively. After entering the nonlinear stage, the development trends of the four curves were similar. The slope of the curve tended to be flat, the load growth was slow in this stage, and the slip gradually increased. This is because the load was slowly transferred from concrete to steel members at this stage. When the peak load was reached, the curve entered the descending stage. At this time, the concrete dowel was crushed, and the load was fully borne by the shear action of penetrating rebars because the steel member had good ductility leading to obvious slip. Owing to the large rigidity of the specimen, the internal steel members were not cut; thus, when the load dropped to a certain range, it was no longer reduced.

The results in Table 3 show that different components have different effects on the growth of the USBC. The USBC of the P-0 specimen can be regarded as being provided by the shear capacity of the concrete dowel as well as the chemical bonding and friction forces of the steel–concrete interface. By contrast, the USBC of P-18 specimen increased by 471.21 kN, which was provided by the shear action of penetrating rebars. Compared with P-18, studs were added to the P-18-S specimen; therefore, the USBC increased by 127.17 kN, which was provided by the shear resistance of the stud. However, the USBC did not increase significantly, because the bearing capacity of the stud itself was lower than that of the perforating steel bar, fewer studs were arranged, and the model used in this test was small. Based on the P-18-S specimen, an end-bearing area was added to the P-18-S# specimen, and the USBC was increased by 256.09 kN, which was provided by the end concrete.

2.5. Effect of Low-Cycle Repeated Load

Low-cycle repeated loads were applied to the WECSC specimens, and then a static load was applied until failure. The low-cycle repeated loading curve of the P-18-S specimen is shown in Figure 12, and a comparison of the USBC and corresponding displacement is presented in Table 4.

Table 4. Comparison result of P-18-S specimen.

Loading Method	USBC/kN	Slippage Corresponding to Peak Load/mm
Static loading	821.43	1.96
Low-cycle repeated loading	816.75	2.39

Figure 12 shows that in the first cycle stage, the initial slope was obvious, which is attributed to the internal of the specimen not being stable, resulting in a certain gap. In the subsequent cycles, the curve presented a linear change, and the slope was consistent and tended to be stable, indicating that all parts of the specimen began to work normally. Analysis of the last section of the unidirectional loading revealed that the load–slip curves

comprised three phases: elastic, nonlinear, and descending. The difference was that the slope of the nonlinear stage was gentle and long because the stiffness of the specimen decreased after several repeated loads.

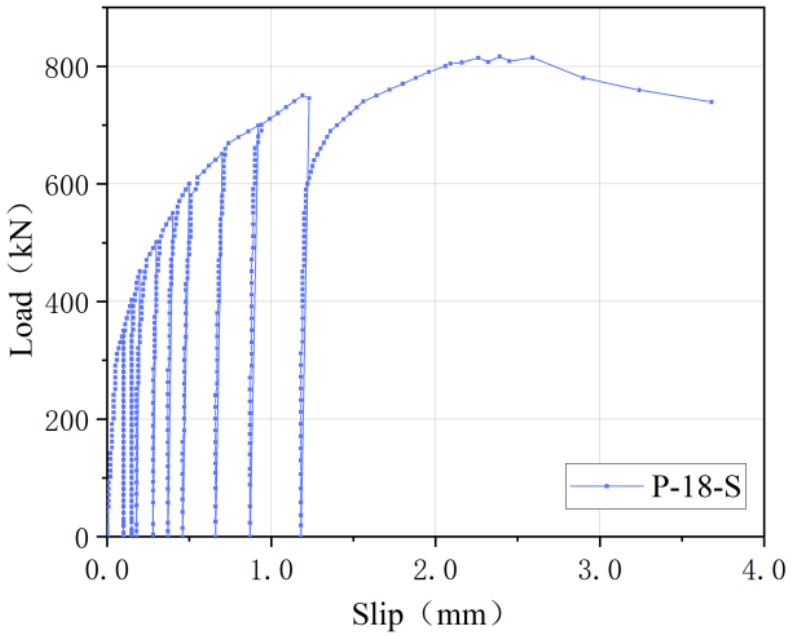

Figure 12. Low-cycle repeated loading load–slip curve.

The USBC of specimen P-18-S, shown in Table 4, decreased, and the ultimate slip increased after repeated loading. The decrease in the value was not large because the number of cycles in this test was small; therefore, the USBC does not change (or decrease) much with small number of repeated loads. The ultimate slip increment was relatively obvious, the slip growth was still large after reaching the peak load. Moreover, it was difficult to enter the obvious decline stage, indicating that the ductility of the specimen exhibited a decreasing trend. Thus, it can be inferred that the specimen may suffer brittle failure after repeated loading.

2.6. Study on Failure Mechanism of Component

The strain evolution at the measuring point of the steel member in the P-18-S specimen was analysed to study the failure mechanism of the member.

The strain evolutions along the lengths of the upper and lower rows of the penetrating rebar are shown in Figure 13a,b, respectively. Overall, the strain changed closer to the middle line of the rebar, which corresponds to a hole. This is because the penetrating rebar directly bears the pressure transmitted by the upper concrete dowel and is simultaneously squeezed by the reaction force of the lower concrete. Before reaching 650 kN, the strain through the steel bar was relatively stable. When the strain exceeded 650 kN, there was a significant increase, indicating that the steel bar began to participate in the shear resistance, and the concrete gradually failed. At approximately 750 kN, the upper row of the steel bars reached the yield, whereas the lower row of the steel bars did not yield until the peak load. This indicated that although the components in the two holes were exactly the same, their stress levels were different, and thus the shear resistance in the lower row holes should be reduced in the subsequent design. The internal force of the specimen is complicated; however, it can be concluded that the steel bar is primarily subjected to pressure, and the failure mode of the steel bar is consistent with the stress process analysed by strain, which is consistent with the numerical analysis value.

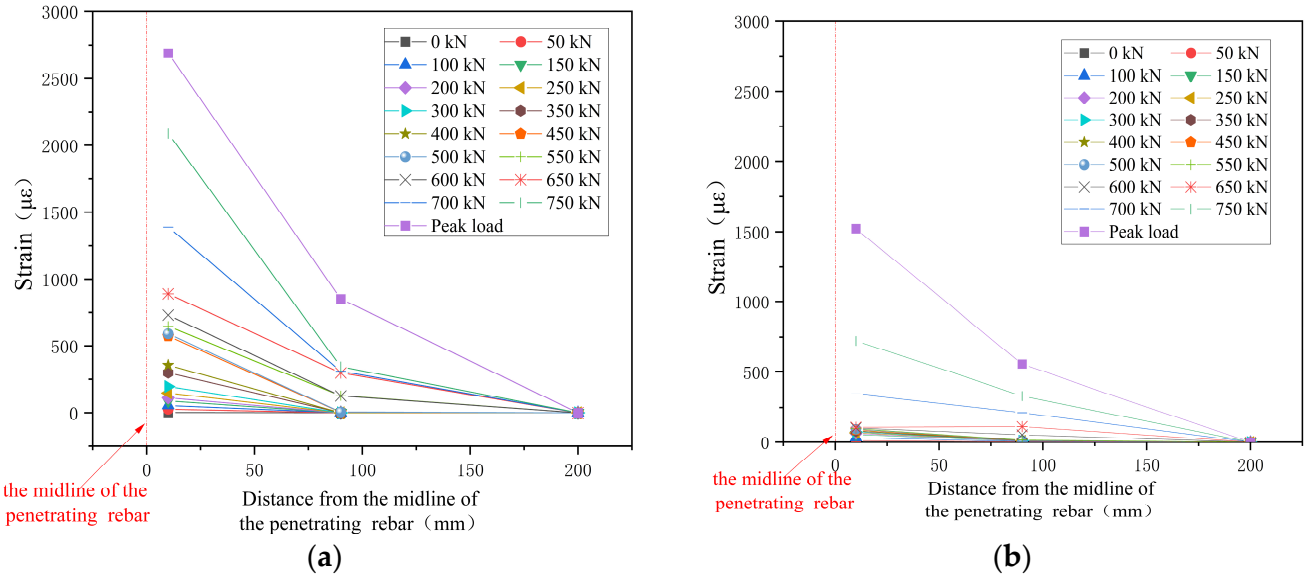

Figure 13. Strain across the length of the steel bar. (**a**) Upper row through rebar; (**b**) lower row through rebar.

Figure 14 shows the deformation of the stud along the length. As is evident, the strain at each stage of the stud root increased more evenly before 600 kN and increased more sharply after 600 kN. However, the strain surge through the reinforcement mentioned above did not occur. This is because the stud root was connected to the steel plate, which resulted in the load being directly transferred to the stud root to move it downward with the steel web. Moreover, the concrete below the stud root produced a reaction force. Strain was experienced at the root of the stud. Simultaneously, the stud root strain was obviously greater than the stud head strain. Thus, the stud root entered the plastic state earlier and yielded at approximately 750 kN. Owing to the restraining effect of the concrete, the stud head exhibited a small strain. It can be observed that after 750 kN, the strain at the stud head exhibited a relatively large increase because the concrete near the root entered the plastic state or failed, and the reaction force no longer increased. To balance the applied load, which continued to increase, the concrete outside the root continued to provide a reaction force. The plastic area of the stud gradually developed from the root to the head.

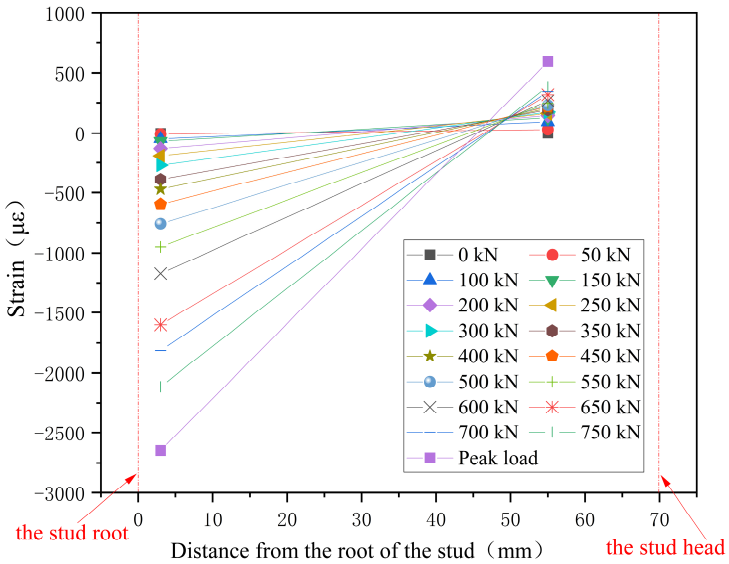

Figure 14. Stud strain along length.

3. Numerical Analysis

3.1. Finite Element Model

The concrete plastic damage model (CDP model in ABAQUS software (2022)) [28] was used to perform the simulation, with a uniaxial concrete stress–strain relationship based on the literature [29]. To balance the calculation accuracy and cost, grids with different size controls should be adopted for each part. Taking the P-18-S test piece as an example, the global seed size of large solid units, such as embedded webs and outsourced concrete, was 20 mm. For a solid unit with a small volume, the global seed size of the penetrating rebar and stud was 5 mm. The grid divisions of each part of the P-18-S specimen model are shown in Figure 15.

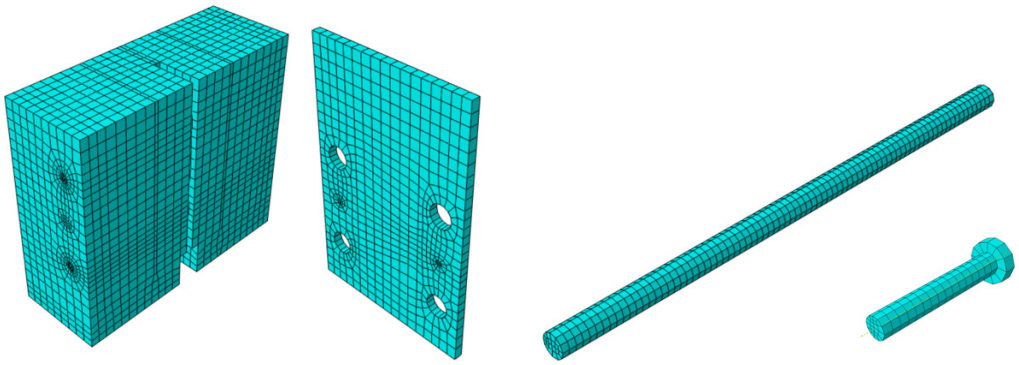

(**a**) (**b**) (**c**) (**d**)

Figure 15. Finite element model. (**a**) Concrete; (**b**) split steel plate; (**c**) penetrating rebar; (**d**) stud.

The stirrup was embedded in the outer concrete by selecting the embedding mode in the constraint. Both the stud and the penetrating rebar were selected to be bound for simulation. Other interactions occurred in the surface–surface contact mode, and the boundary condition was finite slip. The friction coefficient between the embedded web and concrete was 0.1, and that between the inside of the hole and concrete dowel was 0.904 [30]. The friction coefficient between the stud and stress surface of concrete was 0.35 [31]. A complete specimen model was established with six degrees of freedom at the bottom constrained, as shown in Figure 16. According to the actual situation, it is considered that there is no relative displacement or corner at the bottom of the model, and the 6 degrees of freedom at the bottom of the model are constrained to ensure the accuracy of the simulation to the greatest extent.

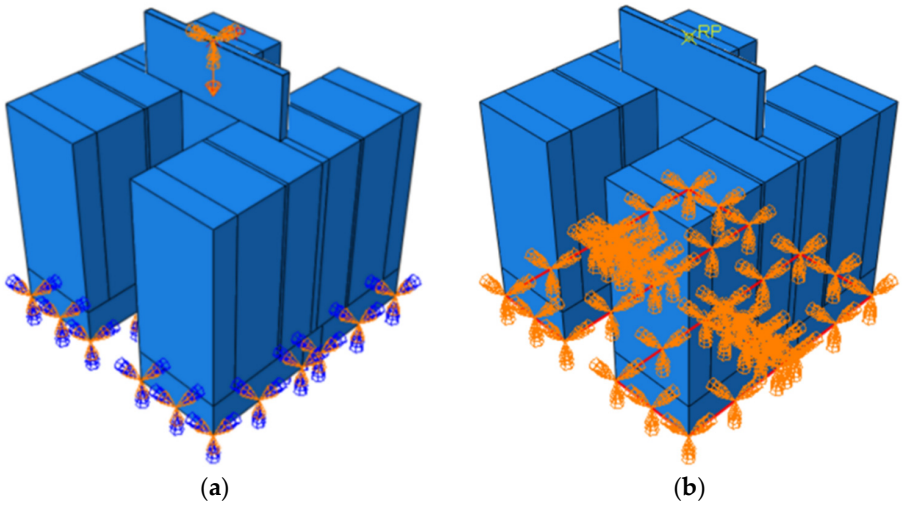

(**a**) (**b**)

Figure 16. Model loading and boundary conditions. (**a**) Top loading point; (**b**) concrete bottom restraint.

The constitutive relation of concrete adopts the CDP model and non-associated flow rule, and its main parameters are shown in Table 5. The constitutive relation of steel adopts the strong elastoplastic model in the twofold model, and its main parameters are shown in Table 6.

Table 5. ABAQUS concrete material parameter setting.

Poisson's Ratio v	Dilation Angle φ	Eccentricity m	f_{bo}/f_{co}	k	Viscosity Coefficient μ
0.2	35°	0.1	1.16	0.6667	0.0001

Table 6. ABAQUS steel parameter setting.

Material	Yield Strength f_y (MPa)	Ultimate Strength f_u (MPa)	Elastic Modulus E_s (GPa)	Poisson's Ratio
Perforated steel plate	345	490	210	0.3
Rebar	426	646	206	0.3
Stud	340	480	206	0.3

3.2. Finite Element Model Verification

3.2.1. Load–Slip Curve Verification

The load–slip curve based on the test results was compared with that of the finite element simulation (Figure 17). The simulated curves of all specimens increased linearly in the elastic stage and gradually decreased in the nonlinear stage. The trend of the simulated curve was consistent with the test curve. A comparison of the curves revealed that the simulated overall stiffness was slightly less than the measured stiffness owing to the presence of many unbalanced forces in the nonlinear analysis process. With the continuous calculation of the model, certain concrete elements began to gradually fail, rendering it difficult to achieve convergence in the iterative calculation. Once the iteration number reached the upper limit, ABAQUS provided the calculation result, which was generally slightly lower than the true value. Further analysis was performed on the error between the finite element simulated and measured USBCs (Table 7).

Table 7. Comparison of USBC values.

Specimen Number	Test Value/kN	Simulated Value/kN	Error/%	Average Error/%
P-0	223.05	214.2	4.0	5.9
P-18	694.26	657.4	5.3	
P-18-S	821.43	787.5	5.4	
P-14-S	745.79	701.7	5.9	
P-22-S	952.37	892.6	6.3	
P-18-S#	1077.52	989.5	8.2	

As shown in Table 7, the overall simulated USBC was less than the measured value, and there were errors between the simulated and measured values. The comparison results showed that the errors ranged as 4.0–8.2%, and the average error of the finite element simulation was 5.9%. This indicated that the simulation results were numerically accurate and reliable.

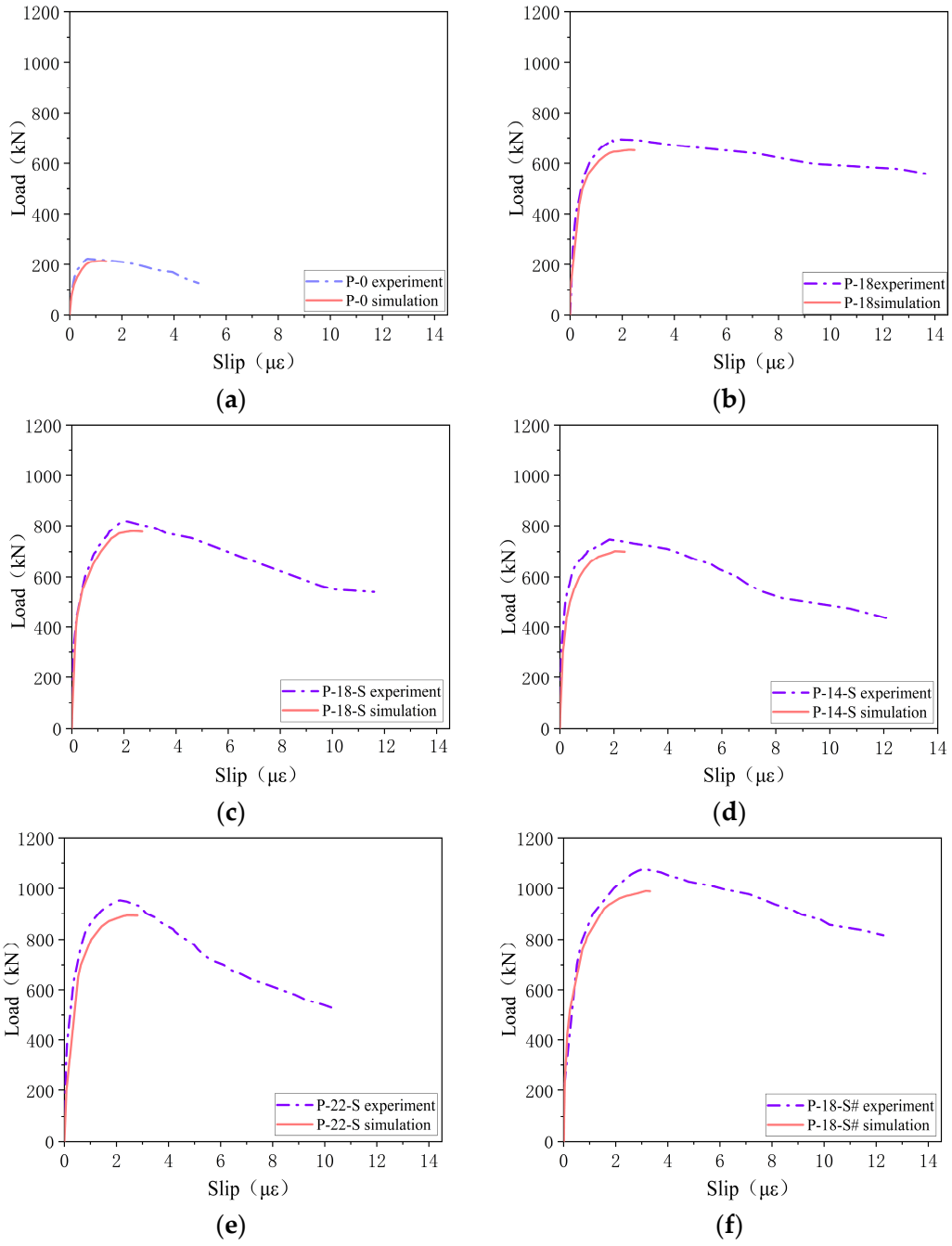

Figure 17. Load–slip curves from tests and simulations. (**a**) Comparison of P-0 test and finite element load-slip curves; (**b**) Comparison of P-18 test and finite element load-slip curves; (**c**) Comparison of P-18-S test and finite element load-slip curves; (**d**) Comparison of P-14-S test and finite element load-slip curves; (**e**) Comparison of P-22-S test and finite element load-slip curves; (**f**) Comparison of P-18-S# test and finite element load-slip curves.

3.2.2. Deformation Verification of Member

The stress nephogram and deformation of the embedded web, penetrating rebar, and stud, in the P-18-S model as an example, is compared and analysed.

The simulated stress, as shown in Figure 18, was mainly distributed above the hole of the embedded steel web and at the joint between the surface and the stud. In practice, the reaction force of the concrete dowel is exerted above the hole of the embedded web, and the shear at the joint between the stud root and embedded web causes stress concentration, indicating that the stress cloud diagram is consistent with the actual stress mechanism. The

maximum stress (325 MPa) occurred at the connection between the surface of the embedded web and stud, and it did not exceed the steel yield strength (340 MPa). Consequently, the web did not buckle, which was consistent with the test results.

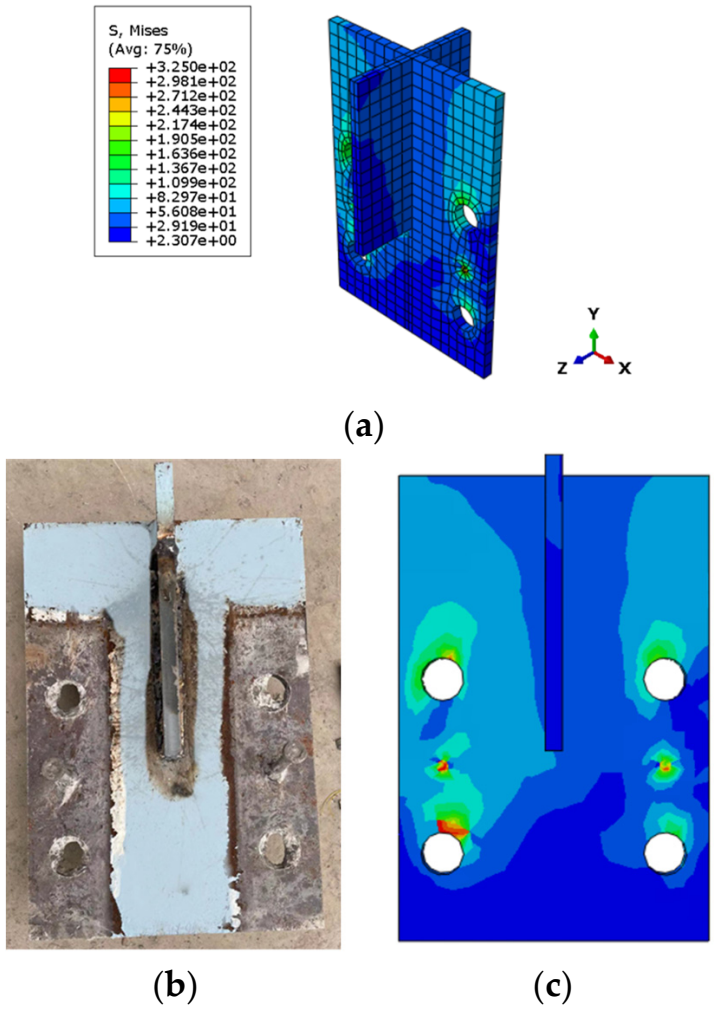

Figure 18. Comparative analysis of perforated steel plate in P-18-S model. (**a**) Stress cloud image of steel web at 0.95 times peak load; (**b**) deformed steel web; (**c**) deformation simulation of steel web.

As shown in Figure 19, the stress concentration occurred in the middle of the penetrating rebar in both the upper and lower rows. The stress decreased from the middle to both ends. Both test and simulation results indicate that the deformation of the upper row penetrating rebar was obviously greater than that of the lower row. The maximum stress value of the upper row of the rebar was 590 MPa, below the ultimate strength (646 MPa). Moreover, there was no fracture. The maximum stress value of the lower bar was 468 MPa, and the yield phenomenon also occurred, later than that of the upper bar.

These phenomena indicate that the simulation results were consistent with the actual force transfer mechanism, and good simulation results were obtained. By observing the evolution animation of the stress cloud map, it was found that the time of obvious stress changes in the penetrating rebars was the same as the time of large amounts of damage in the concrete. This indicated that after the gradual failure of the concrete, the penetrating rebars began to provide shear resistance.

Figure 20 shows the stress cloud map of the stud at 0.95 times the peak load and the comparison between the actual deformation tested and the simulated deformation. The maximum stress of stud reached 436 MPa at the root, below the ultimate strength

(480 MPa). Thus, the root of the stud had yielded instead of cut, which is consistent with the test results.

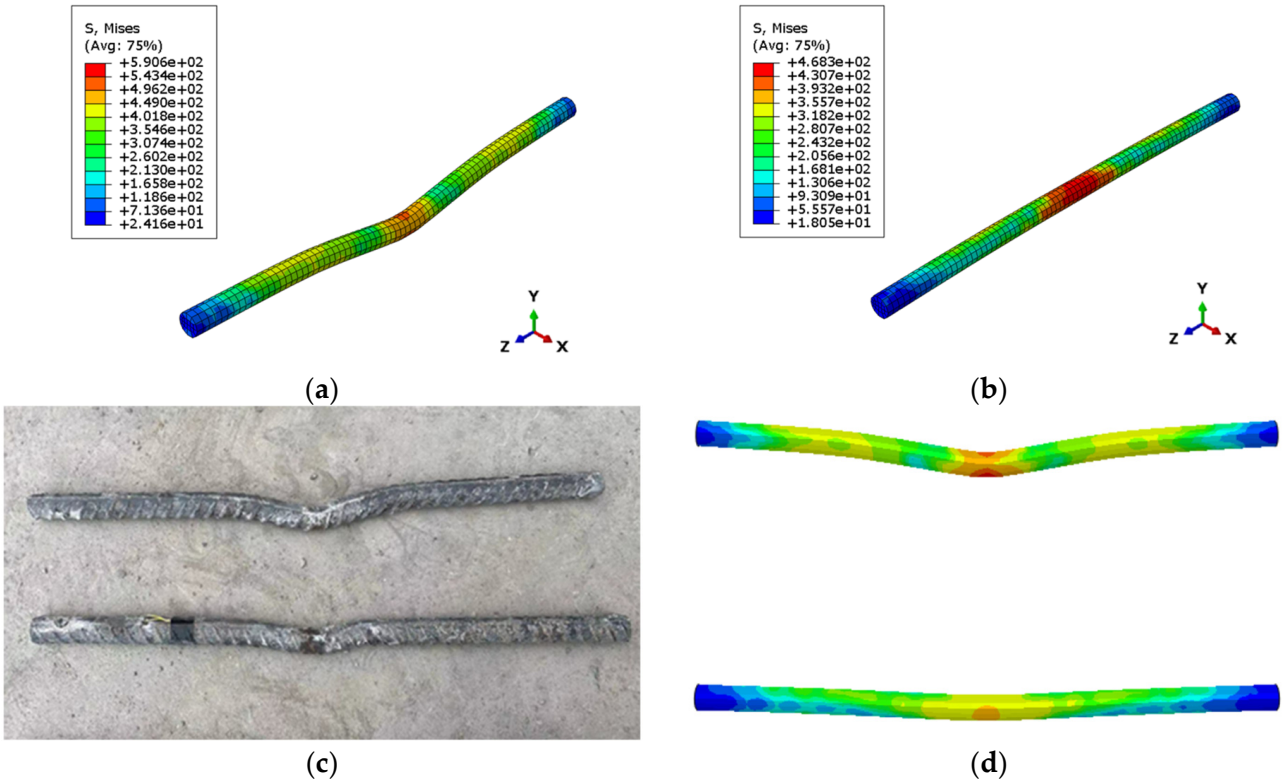

Figure 19. Comparison analysis diagram of steel bar through P-18-S model. (**a**) Stress cloud diagram of the upper row penetrating rebar at 0.95 times the peak load; (**b**) stress cloud diagram of the lower row penetrating rebar at 0.95 times the peak load; (**c**) deformation of the penetrating rebar in the test; (**d**) through steel deformation in simulation.

By observing the evolution animation of the stress nephogram, it was found that the shear action provided by the stud was very early, indicating that its shear action was not completely controlled by the concrete, but also depended on the embedded web.

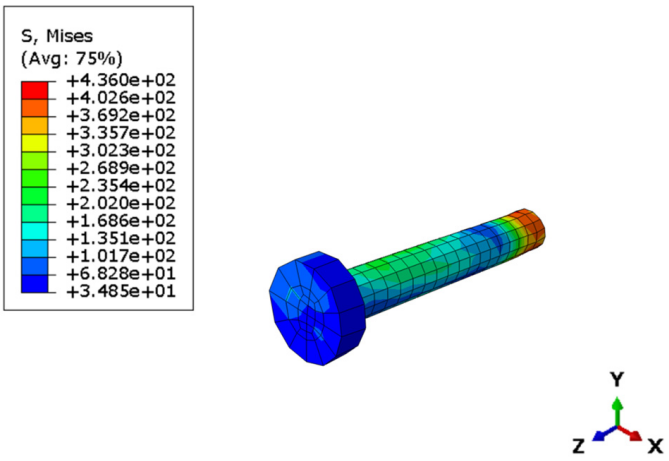

Figure 20. *Cont.*

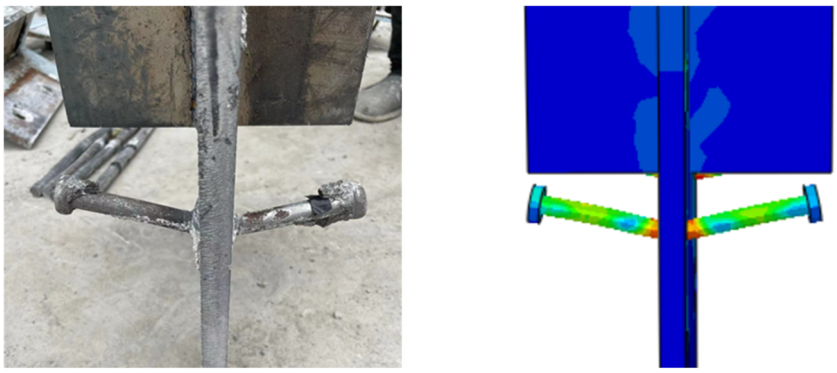

(**b**) (**c**)

Figure 20. Comparison analysis diagram of stud in P-18-S model. (**a**) Stud stress cloud diagram at 0.95 times peak load; (**b**) stud deformation in the test; (**c**) stud deformation in simulation.

3.3. Finite Element Parameter Analysis

Three parameters were set for analysis, including the thickness of the embedded web, the hole diameter, and the diameter of the stud. After finite element analysis, it was concluded that (1) the USBC of the model increased slightly with increase in web thickness; (2) the larger the hole diameter, the greater the lifting effect of the USBC, and an increase in the diameter of the penetrating rebar weakened the lifting effect of the hole diameter; (3) the USBC increased when the stud diameter increased.

4. Calculation Equation of USBC

4.1. Shear Resistance Mechanism of WECSC

In the test, a specimen with an end-bearing area was set up to study the effect of the concrete end bearing on the USBC. However, in the actual layout, the WECSC is generally arranged in a continuous manner, so there is no end bearing area. Therefore, the design of the shear strength does not consider the end bearing effect. There are certain adhesive friction effects between the concrete and steel plate, and owing to it values being very small, it is usually ignored in the calculation of PBL shear connectors. However, owing to the difference in the structure of the composite shear connectors embedded with a web plate, the contact area between the concrete and steel plate was increased by directly embedding the web plate into the concrete plate, and no oil treatment was performed on the contact surface in the test. Therefore, in this study, the adhesive and friction forces were considered in the calculation of the shear capacity.

The shear bearing mechanism of WECSC is shown in Figure 21. The USBC P_n is primarily a linear superposition of the following four parts: (1) P_b caused by chemical adhesion and friction between the concrete and embedded web, (2) P_s owing to the stud, (3) P_c owing to concrete dowels, and (4) P_{tr} caused by penetrating steel bars.

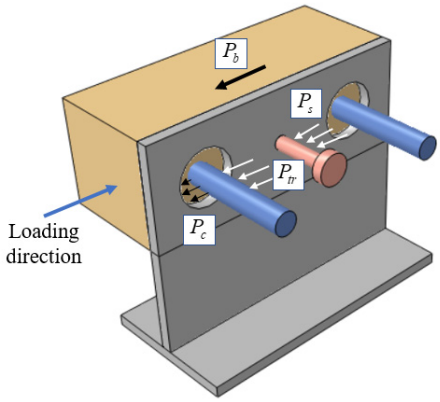

Figure 21. Shear bearing mechanism of WECSC.

Therefore, the equation for calculating the USBC P_n of the WECSC can be expressed as follows:

$$P_n = P_b + P_s + P_c + P_{tr} \quad (1)$$

4.2. P_b Calculation Equation

P_b represents the shear capacity provided by the chemical adhesion and friction between the concrete and embedded web. Its value is primarily determined by the contact area between the concrete and web and the strength of the concrete. Considering the He S formula [32], the calculation equation of P_b can be expressed as follows:

$$\begin{cases} P_b = \tau_b A_b \\ \tau_b = -0.022 f_c + 0.306\sqrt{f_c} - 0.573 \\ A_b = 2 \times \left(t_m h_m - n\pi d^2/4\right) \end{cases} \quad (2)$$

where τ_b is the friction force between concrete and shear connector surface per unit area (N/mm^2), A_b is the contact area between concrete and perforated steel plate (mm^2), t_m is the embedment depth of steel web (mm), h_m is the steel web embedding height (mm), f_c is the compressive strength of concrete axis (N/mm^2), n is the number of holes, and d his the hole diameter (mm).

4.3. P_s Calculation Equation

Currently, the calculation method of the USBC for stud connectors is included in many national codes, and many representative calculation equations have been proposed by scholars. Because of the different parameters considered in the derivation and calculation methods, and the differences in the tests, the existing equations for calculating the USBC of the stud connector are not completely consistent with the calculation results. However, the shear mechanisms based on them are the same.

Equations proposed by the Oehler's formula [33], Eurocode 4 [34], AISC2005 [35], the literature [6], and Shi Weihua's formula [36] have been compared and analysed.

For the USBC of the WECSC, according to the test results, we consider the smaller result reference equation in the literature [6], introduce the test conversion coefficient α_s, and obtain α_s = 0.98 through the test data. Therefore, P_s can be expressed:

$$\begin{cases} P_s = 1.19\alpha_s A_s f_u \left(\frac{E_c}{E_s}\right)^{0.2} \left(\frac{f_{cu}}{f_u}\right)^{0.1} = 1.17 A_s f_u \left(\frac{E_c}{E_s}\right)^{0.2} \left(\frac{f_{cu}}{f_u}\right)^{0.1} \\ A_s = n_s \pi d_s^2/4 \end{cases} \quad (3)$$

where f_u is the minimum ultimate tensile strength of stud (N/mm^2), f_{cu} is the compressive strength of concrete cube (N/mm^2), A_s is the cross-sectional area (mm^2) of the part connecting the stud and the interface, n_s is the number of studs, d_s is the stud bottom diameter (mm), E_c is the elastic modulus of concrete (N/mm^2), and E_s is the stud elastic modulus (N/mm^2).

4.4. P_c Calculation Equation

P_c represents the shear capacity of the concrete dowels. Although the influence of the thickness of the embedded web was studied using finite element analysis, it was found to have minimal influence. Moreover, the reduced coefficient related to the thickness of the embedded web could not be directly extracted in this test; therefore, its value was expressed by multiplying the concrete dowel section area by the shear strength.

According to the principles presented in the literature [37], the shear strength of concrete under pure shear is $\tau_c = 0.39 f_{cu}^{0.57}$. However, in this research, the concrete dowel was subjected to double shear; thus, this shear strength value should be considered as 2 times when under pure shear. The concrete in the hole was constrained by embedded web, penetrating rebar, and other conditions; thus, its strength was improved. Therefore,

the lifting coefficient α_c was introduced and α_c = 3.55 was obtained through the test data. Therefore, the calculation equation of P_c can be expressed:

$$\begin{cases} P_c = 2\alpha_c A_c \tau_c = 2.77 A_c f_{cu}^{0.57} \\ A_c = n\pi(d - d_{tr})^2/4 \end{cases} \quad (4)$$

where f_{cu} is the compressive strength of concrete cube (N/mm^2) and A_c is the concrete dowel area (mm^2).

4.5. P_{tr} Calculation Equation

P_{tr} represents the shear strength of the penetrating rebar. The calculation formulae for the USBC of the PBL shear connectors in Eurocode 4 [34], the Leonhardt formula [38], Oguejiofor formula [39], He S formula [32], and Hu Jianhua formula [40] have been referred.

According to the force transmission mechanism analysed above, the shear bearing effect of the lower row of penetrating rebars was smaller than that of the upper row of penetrating rebars. Therefore, the shear bearing capacity of multiple rows of penetrating rebars cannot be determined by a simple multiple relation. Thus, the test conversion coefficient α_{tr} must be introduced and obtained as $\alpha_{tr} = -0.0375\mathrm{d_{tr}}+1.76$ through the test data. In addition, the shear strength of the steel bar in the pure shear state is $\tau_{tr} = f_y/\sqrt{3}$.

Therefore, the calculation equation of P_{tr} can be expressed:

$$\begin{cases} P_{tr} = 2\alpha_{tr} A_{tr} \tau_{tr} = 1.155(1.76 - 0.0375 d_{\mathrm{tr}}) A_{tr} f_y \\ A_{tr} = n\pi d_{tr}^2/4 \end{cases} \quad (5)$$

where f_y is the yield strength of steel bar (N/mm^2), A_{tr} is the cross-sectional area of the steel bars (mm^2), and d_{tr} is the diameter of the penetrating rebar (mm).

4.6. General Equation of Shear Capacity

The equation for calculating the USBC of the WECSC is expressed as follows:

$$\begin{aligned} P_n \quad &= \left(2t_m h_m - n\pi d^2/2\right)\left(-0.022 f_c + 0.306\sqrt{f_c} - 0.573\right) \\ &+0.69 n\pi (d - d_{tr})^2 A_c f_{cu}^{0.57} \\ &+0.29 n\pi d_{tr}^2 (1.76 - 0.0375 d_{\mathrm{tr}}) A_{tr} f_y \\ &+0.29 n_s \pi d_s^2 f_u \left(\frac{E_c}{E_s}\right)^{0.2} \left(\frac{f_{cu}}{f_u}\right)^{0.1} \end{aligned} \quad (6)$$

Equation (6) was used to calculate the WECSC specimens in this test and compared with the test and finite element simulation results (Table 8). The results show that there is minimal error between the results obtained using Equation (6) and the test results, with a maximum error of 9.66%. The variance in results was analysed, and the *p*-value was 0.91, indicating that there was no significant difference between the results obtained using Equation (6) and the experimental values. A correlation analysis was performed on the results, and the correlation coefficient R^2 = 0.99 was obtained, indicating that the results of the two groups were very similar, and results using Equation (6) were consistent with the experimental values.

Table 8. Comparison of the results of the derived equations with the experimental results.

Specimen Number	Test Value/kN	Value Based on Equation (6)/kN	Error/%	*p*-Value	R^2
P-0	223.05	223.14	−0.04	0.91	0.99
P-18	694.26	654.21	5.76		
P-18-S	821.43	822.64	−0.15		
P-14-S	745.79	673.73	9.66		
P-22-S	952.37	961.29	−0.94		

To further verify Equation (6) for the WECSC, it was necessary to compare it with a large amount of data. However, because the specific structure of the composite shear connectors with an embedded web was proposed in this study and no test specimen with the same structure has been found in the existing literature, 22 models considering different parameters were simulated using Abaqus. The model number was CxSyHzPm (x, y, z, and m represent the concrete strength, stud type, open-hole aperture, and diameter of the penetrating rebar, respectively). The simulation results are presented in Table 9.

Table 9. Finite element simulation result.

Model Number	Simulated Values/kN	Model Number	Simulated Values/kN
C50S13H34P14	652.92	C40S13H44P22	899.15
C50S13H54P14	761.15	C50S16H44P18	837.45
C50S13H34P18	748.81	C50S19H44P18	912.76
C50S13H54P18	833.12	C50S10H44P18	783.37
C50S13H34P22	863.63	C40S16H44P9	656.91
C50S13H54P22	934.83	C40S10H44P9	533.47
C30S13H44P14	692.64	C40S19H44P9	680.23
C40S13H44P14	699.84	C40S13H44P9	584.98
C30S13H44P18	723.62	C40S13H24P9	403.15
C40S13H44P18	729.68	C30S13H24P9	384.96
C30S13H44P22	892.76	C50S13H24P9	427.83

Figure 22 shows a comparison between the values calculated using Equation (6), the test value, and the finite element simulation value. It is evident these three values can be well matched with each other, with a correlation coefficient of $R^2 = 0.93$.

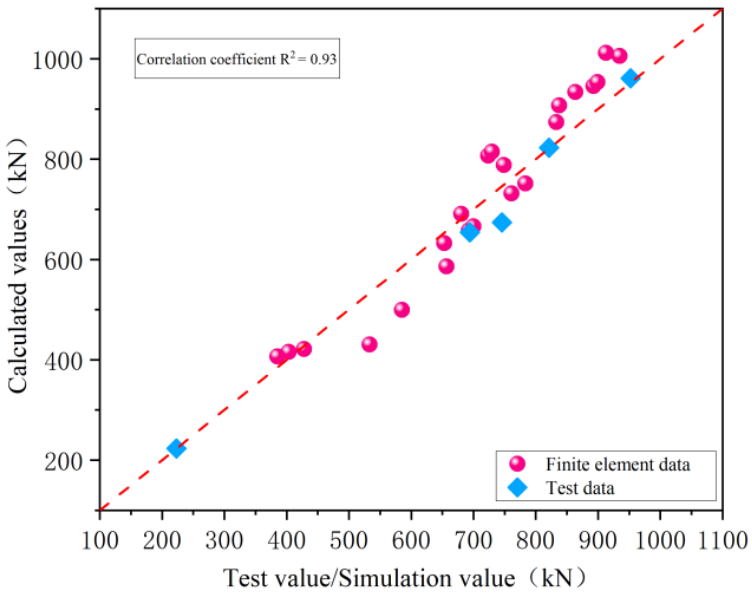

Figure 22. Comparison of the calculated value with the test and simulated values.

In summary, Equation (6) derived in this study has a clear physical meaning, and through a comparative analysis, it was found that it can predict the USBC of the WECSC like those mentioned in this article.

5. Conclusions

This study proposed a shear connector, the WECSC, to conduct push-out test studies on its USBC. Seven specimens in six categories were set up, the failure mode, load–slip curve, and load–strain curve were analysed. Numerical and parameter analyses were performed and verified using the test results. The shear mechanism of the WECSC was summarised, and a new equation for calculating the USBC was derived.

(1) The shear stiffness of the WECSC was high, the ultimate slip was low, and the shear connector exhibited good ductility after reaching the ultimate load. The failure forms were the partial crushing of the concrete dowel and splitting of the outer concrete. The penetrating rebars and studs were bent and shear-deformed, without cut. This indicated that the shear connectors could still maintain a good shear bearing capacity after exceeding the ultimate load, and every component of the shear connectors was fully used.

(2) The force transfer mechanism of the WECSC was studied based on tests and numerical analyses. After the failure of the concrete dowel, the penetrating rebars gradually began to participate in the shear resistance. Because of the position of the load, yield deformation occurred at the midpoint of the steel bars, and because the load was transmitted from top to bottom, the upper row of steel bars yielded earlier and entered the strengthening stage. Simultaneously, the stud was driven downward by the steel plate, the concrete below the root produced a reaction, and the head was constrained by the concrete. Thus, the stud root produced an obvious bending shear deformation. As the load continued to increase, the plastic area of the stud gradually began from the root and developed towards the head.

(3) The proportion of USBC of different shear members was different. The proportion of the penetrating rebar being the largest, followed by the end-bearing area, and that of the studs is the smallest. The ultimate slip and USBC of the WECSC increased with an increase in the diameter of the penetrating rebar, not linear. The larger the hole diameter, the greater the lifting effect of the USBC, whereas an increase in the diameter of the penetrating rebar weakened the lifting effect of the hole diameter. After repeated loading, the USBC of the specimen decreased, the ultimate slip increased, and the ductility of the specimen decreased.

(4) The USBC of the WECSC was mainly provided by the chemical bonding force and friction among the concrete, embedded web, stud, concrete dowel, and penetrating rebar. A new suitable calculation equation for the USBC was derived. The correlation coefficient between the calculated, experimental, and numerically simulated values was 0.93, indicating that the calculation method was more accurate and had a certain reference value.

Author Contributions: Conceptualization, X.X., H.T. and Y.W.; Methodology, X.X., H.T., Y.W. and Y.Z.; Software, S.H.; Formal analysis, T.S. and Y.W.; Investigation, X.X.; Resources, Y.Z.; Data curation, T.S. and S.H.; Writing—original draft, T.S. and S.H.; Writing—review & editing, X.X.; Supervision, H.T. and Y.Z. All authors have read and agreed to the published version of the manuscript.

Funding: This research was funded by [Chongqing Municipal Education Commission] grant number [KJZD-K202300702], [National Key R&D Program Fund] grant number [2022YFB2302501-3], [State Key Laboratory of Mountain Bridge and Tunnel Engineering] grant number [SKLBT-2103]. The APC was jointly funded by the above three projects.

Institutional Review Board Statement: Not applicable.

Informed Consent Statement: Not applicable.

Data Availability Statement: The raw data supporting the conclusions of this article will be made available by the authors on request.

Conflicts of Interest: Author Yuxiao Wang was employed by the company "Construction Branch of State Grid Sichuan Electric Power Company". The remaining authors declare that this research was

conducted in the absence of any commercial or financial relationships that could be construed as a potential conflict of interest.

References

1. Xu, X.; He, D.; Zeng, S.; He, W.; Tan, H.; Yu, Z. Effect of concrete cracks on the corrosion of headed studs in steel and concrete composite structures. *Constr. Build. Mater.* **2021**, *293*, 123440. [CrossRef]
2. Wang, Y.-H.; Nie, J.-G.; Li, J.-J. Study on fatigue property of steel–concrete composite beams and studs. *J. Constr. Steel Res.* **2014**, *94*, 1–10. [CrossRef]
3. Lowe, D.; Roy, K.; Das, R.; Clifton, C.G.; Lim, J.B.P. Full scale experiments on splitting behaviour of concrete slabs in steel concrete composite beams with shear stud connection. *Structures* **2020**, *23*, 126–138. [CrossRef]
4. Bonilla, J.; Bezerra, L.M.; Mirambell, E.; Massicotte, B. Review of stud shear resistance prediction in steel-concrete composite beams. *Steel Compos. Struct.* **2018**, *27*, 355–370. [CrossRef]
5. Xu, Y.; Liu, X.; Wang, B.; Yi, X. Residual mechanical properties of composite beams with PBL connectors under fatigue loads. *Structures* **2023**, *51*, 185–195. [CrossRef]
6. *GB50917-2013*; Ministry of Housing and Urban-Rural Development of the People's Republic of China, Code for Design of Steel and Concrete Composite Bridges. China Planning Press: Beijing, China, 2013.
7. Wu, F.; Tang, W.; Xue, C.; Sun, G.; Feng, Y.; Zhang, H. Experimental investigation on the static performance of stud connectors in steel-hsfrc composite beams. *Materials* **2021**, *14*, 2744. [CrossRef] [PubMed]
8. Peng, K.; Liu, L.; Wu, F.; Wang, R.; Lei, S.; Zhang, X. Experimental and Numerical Analyses of Stud Shear Connectors in Steel–SFRCC Composite Beams. *Materials* **2022**, *15*, 4665. [CrossRef] [PubMed]
9. Zhang, H.; Ling, Z. Finite Element Modeling on Shear Performance of Grouted Stud Connectors for Steel–Timber Composite Beams. *Materials* **2022**, *15*, 1196. [CrossRef] [PubMed]
10. Wu, F.-W.; Feng, Y.-P.; Dai, J.; Wang, G.-Q.; Zhang, J.-F. Study on mechanical properties of stud shear connectors in steel-UHPC composite structures. *Gongcheng Lixue/Eng. Mech.* **2022**, *39*, 222–234. [CrossRef]
11. Wang, X.; Zhu, B.; Cui, S.; Lui, E.M. Experimental Research on PBL Connectors Considering the Effects of Concrete Stress State and Other Connection Parameters. *J. Bridge Eng.* **2018**, *23*, 04017125. [CrossRef]
12. Yang, Y.; Chen, Y. Experimental Study on Mechanical Behavior of PBL Shear Connectors. *J. Bridge Eng.* **2018**, *23*, 04018062. [CrossRef]
13. Deng, W.; Xiong, Y.; Liu, D.; Zhang, J. Static and fatigue behavior of shear connectors for a steel-concrete composite girder. *J. Constr. Steel Res.* **2019**, *159*, 134–146. [CrossRef]
14. Li, Z.; Zhao, C.; Deng, K.; Wang, W. Load Sharing and Slip Distribution in Multiple Holes of a Perfobond Rib Shear Connector. *J. Struct. Eng.* **2018**, *144*, 04018147. [CrossRef]
15. Kim, H.-Y.; Jeong, Y.-J. Experimental investigation on behaviour of steel-concrete composite bridge decks with perfobond ribs. *J. Constr. Steel Res.* **2006**, *62*, 463–471. [CrossRef]
16. Wu, F.; Liu, S.; Xue, C.; Yang, K.; Feng, Y.; Zhang, H. Experimental study on the mechanical properties of perfobond rib shear connectors with steel fiber high strength concrete. *Materials* **2021**, *14*, 3345. [CrossRef] [PubMed]
17. Schmitt, V.; Seidl, G.; Hever, M.; Zapfe, C. The new road bridge over the railway line next to Pöcking applied to a new construction method for composite bridges Verbundbrücke Pöcking—Innovative VFT-Träger mit Betondübeln. *Stahlbau* **2004**, *73*, 387–393. [CrossRef]
18. Park, C.S.; Yi, H.J.; Kim, Y.-T.; Han, S.W.; Lee, T.; Moon, Y.H. Tempcore Process Simulator to Analyze Microstructural Evolution of Quenched and Tempered Rebar. *Appl. Sci.* **2019**, *9*, 2938. [CrossRef]
19. Akbarpour, M.R.; Mashhuriazar, A.; Daryani, M. Experimental and Numerical Investigation on the Effect of the Tempcore Process Parameters on Microstructural Evolution and Mechanical Properties of Dual-Phase Steel Reinforcing Rebars. *Met. Mater. Int.* **2021**, *27*, 4074–4083. [CrossRef]
20. Li, G.; Si, L.; Li, X.; Li, L. Experimental Study on Shear Capacity of Embedded Composite Beam with Notched Web. *J. Tongji Univ. (Nat. Sci.)* **2011**, *39*, 482–487. [CrossRef]
21. Li, G.Q.; Li, L.; Li, X.H.; Si, L.-J. Theoretical and experimental analysis of bending behavior of composite beam with notched web. *Tumu Jianzhu Yu Huanjing Gongcheng/J. Civ. Archit. Environ. Eng.* **2011**, *33*, 1–7+30. [CrossRef]
22. Naito, C.J.; Hendricks, R.; Sause, R.; Cercone, C. Composite Steel Tee Concrete Deck Bridge System: Design, Fabrication, and Full-Scale Verification. *J. Bridge Eng.* **2021**, *26*, 04020109. [CrossRef]
23. AASHTO. *AASHTO LRFD Bridge Design Specifications*; Seventh Edition with 2016 Interim Revisions; AASHTO: Washington, DC, USA, 2016.
24. Yang, Y.; Sun, T.; Han, J. Study on Shear Brhavior of eb-Embedded U-ShaprdSteel-Concrete Composite Beam. *Eng. Mech.* **2022**, *39*, 120–136.
25. Cercone, C.; Naito, C.J.; Hendricks, R.; Sause, R. Composite Steel Tee Concrete Deck Bridge System: Performance of Interface Shear Connection. *J. Bridge Eng.* **2021**, *26*, 04021003. [CrossRef]
26. *JTG/T D64-01-2015*; CCCC Highway Consultants Co. Specifications for Design and Construction of Highway Steel-Concrete Composite Bridge. China Communications Press: Beijing, China, 2015.

27. *GB/T10433-2002*; Cheese Head Studs for Arc Stud Welding. Inspection and Quarantine of the People's Republic of China General Administration of Quality Supervision: Beijing, China, 2022.
28. Franchi, A.; Napoli, P.; Crespi, P.; Giordano, N.; Zucca, M. Unloading and Reloading Process for the Earthquake Damage Repair of Ancient Masonry Columns: The Case of the Basilica di Collemaggio. *Int. J. Archit. Herit.* **2021**, *16*, 1683–1698. [CrossRef]
29. *GB 50010-2010*; Ministry of Housing and Urban-Rural Development of the People's Republic of China, Code for Design of Concrete Structures. China Architecture & Building Press: Beijing, China, 2014.
30. Su, Q.; Du, X.; Li, C.; Jiang, X. Tests of Basic Physical Parameters of Steel-concrete Interface. *J. Tongji Univ. (Nat. Sci.)* **2016**, *44*, 499–506.
31. Bing, W. Study on Residual Mechanical Properties of Steel-Concrete Composite Beam Bridges Based on Cumulative Fatigue Damnification. Ph.D. Thesis, Southeast University, Nanjing, China, 2017.
32. He, S.; Fang, Z.; Fang, Y.; Liu, M.; Liu, L.; Mosallam, A.S. Experimental study on perfobond strip connector in steel–concrete joints of hybrid bridges. *J. Constr. Steel Res.* **2016**, *118*, 169–179. [CrossRef]
33. Oehlers, D.J.; Johnson, R.P. Strength of Stud Shear Connections in Composite Beams. *Struct. Eng. Part B RD Q.* **1987**, *65 B*, 44–48. [CrossRef]
34. *EC 4, Structural Steelword Eurocodes: Development of a Trans-National Approach*; Publication Office of the European Union: Luxembourg, 2001.
35. AISC. *Specification for the Design, Fabrication and Erection of Structural Steel for Buildings*; AISC: Chicago, IL, USA, 1969.
36. Shi, W.; Chen, L.; Chen, D. Reliability Analysis of Shear Capacity of Stud Shear Connectors. *J. Hunan Univ. Sci. Technol. (Nat. Sci. Ed.)* **2019**, *34*, 28–35. [CrossRef]
37. Guo, Z.H. *Principle of Reinforced Concrete*; Tsinghua University Press: Beijing, China, 2013.
38. Leonhardt, F.; Andrä, W.; Andrä, H.-P.; Harre, W. Neue vorteilhaftes fur Stahlverbund-Tragwerke mit hoher Dauerfestigkeit. *Beton Und Stahlbetonbau* **1987**, *82*, 325–331. [CrossRef]
39. Oguejiofor, E.C.; Hosain, M.U. A parametric study of perfobond rib shear connectors. *Can. J. Civ. Eng.* **1994**, *21*, 614–625. [CrossRef]
40. He, J.; Ye, M.; Huang, Q. Experiment on Bearing Capacity of PBL Shear Connectors. *J. Constr. Steel Res.* **2006**, *33*, 65–72. [CrossRef]